RSC Advances

PAPER

View Article Online
View Journal | View Issue

Cite this: *RSC Adv.*, 2024, **14**, 13808

Colorimetric detection of Hg^{2+} based on the enhanced oxidase-mimic activity of CuO/Au@$Cu_3(BTC)_2$ triggered by Hg^{2+}†

Min Yang, [a] Jian Wang, *[b] Xuan Xue[a] and Hechun Jiang *[c]

Received 14th March 2024
Accepted 17th April 2024

DOI: 10.1039/d4ra01953a

rsc.li/rsc-advances

It is imperative to develop a rapid detection method for Hg^{2+} due to its harm to human health and the ecological environment. In this research, CuO/Au@$Cu_3(BTC)_2$ was synthesized through reducing $HAuCl_4$ by Cu_xO@$Cu_3(BTC)_2$, which was obtained by reducing $Cu_3(BTC)_2$ with hydrazine hydrate. The oxidase-mimic activity of CuO/Au@$Cu_3(BTC)_2$ can be enhanced by Hg^{2+} through forming a Au–Hg alloy. Therefore, a colorimetric method was designed for Hg^{2+} detection with a linear relationship in the 0.05–25 μM range and a limit of detection of 9.7 nM. This strategy exhibited a strong selectivity to Hg^{2+} and was applied in a real water sample with reliable recoveries. This work provides a possibility for the rapid detection of Hg^{2+}.

1. Introduction

Heavy metal pollution has become a tremendous environmental issue, due to its harmful effects on the environment and organisms.[1,2] Mercury ions (Hg^{2+}), with a high toxicity, are one of the proverbial representatives of heavy metal pollutants, which are widely distributed in water and soil.[3–5] Mercury ions cannot be eliminated from the body through their metabolism and may cause damage to the immune system, nervous system, heart, and kidneys.[6,7] According to the World Health Organization, the maximum concentration limit of Hg^{2+} in drinking water is 30 nM.[8] Therefore, the identification and determination of Hg^{2+} in water is extremely crucial for evaluating its toxicity and health risk.[9,10] To date, various methods have been reported for Hg^{2+} detection, including inductively coupled plasma mass spectrometry (ICP-MS), atomic absorption spectroscopy (AAS), electrochemical detection, surface-enhanced Raman scattering (SERS), fluorescence and colorimetric assays.[11–20] Among these techniques, colorimetric assays based on nanozymes have attracted widespread attention due to the unique properties of high precision, simple operation, low cost, fast response, and naked eye detection.[21,22]

Many researchers are dedicated to developing effective colorimetric assays based on enzyme-mimetic reactions for the sensitive and selective detection of mercury ions.[23,24] Generally, Hg^{2+} can either enhance or inhibit the enzyme-mimetic activities of nanozymes and make it realize the colorimetric detection of Hg^{2+} based on the 3,3,5,5-tetramethylbenzidine (TMB) chromogenic system.[25–29] One way to design the colorimetric strategy for Hg^{2+} detection is based on the robust interaction between Hg and S (or Se).[25–27] Liu *et al.*, using an N, S co-doped carbon-$Co_6Ni_3S_8$ nanocomposite (NSC/$Co_6Ni_3S_8$) as an oxidase-like nanozyme, developed a smartphone-based colorimetric sensor for Hg^{2+} detection.[25] Hg^{2+} served as a trigger center by forming HgS on the nanozyme, which led to an enhanced oxidase-like activity in this colorimetric system. Similarly, Luo *et al.* designed a colorimetric platform for Hg^{2+} detection based on the Hg^{2+}-triggered oxidase-like activity of $NiSe_2$.[26] Li *et al.* found a novel "on–off–on" colorimetric strategy for Hg^{2+} based on the Fe–N/S–C nanozyme-glutathione (GSH)-TMB system.[27] In this colorimetric system, glutathione, an inhibitor for the oxidation of TMB, Hg^{2+}, exerts a relieving role through the strong interaction between Hg^{2+} and glutathione to restore the oxidase-like activity of the nanozyme. Another strategy is to utilize the amalgam reaction between Hg^{2+} and noble metal (such as Ag, Au, Pd, Pt, *etc.*) nanozymes.[22,28,29] Cai *et al.* reported a colorimetric sensing method of Hg^{2+} based on the enhanced peroxidase-mimics of bimetallic Ag/Cu nanoclusters through the reaction between Hg^{2+} and Ag/Cu nanoclusters.[28] Xiang *et al.* reported an ultrasensitive detection of Hg^{2+} based on the inhabitation to the peroxidase-like activity of silica-loading with Pt nanoparticles.[29]

Recently, metal–organic frameworks (MOFs) have been widely investigated in the detection of Hg^{2+}, owing to the excellent properties of controllable pore size, large specific surface area, and exposed active sites.[20,30–33] For example, Fu *et al.* established an electrochemical sensor based on thioether-modified Zr-MOF for Hg^{2+} detection.[31] Compared with bare Zr-

[a]School of Pharmacy, Anhui University of Chinese Medicine, Hefei, 230012, China
[b]School of Chemistry and Chemical Engineering, Shandong University, Jinan, 250100, China. E-mail: prawang@sdu.edu.cn
[c]State Key Laboratory of Crystal Materials and Institute of Crystal Materials, Shandong University, Jinan, 250100, China. E-mail: jianghechun@sdu.edu.cn

† Electronic supplementary information (ESI) available. See DOI: https://doi.org/10.1039/d4ra01953a

MOF, the electrochemical sensors based on thioether-modified Zr-MOF show a high selectivity and linear detection of mercury ions due to strong binding between thioether and mercury ions. Furthermore, Zhang *et al.* developed an ultra-sensitive fluorescence sensor based on a AuNCs/Ce-MOF hybrid for Hg^{2+} detection.[20] The sensor exhibited a better linear range and a lower detection limit for Hg^{2+} detection compared with that of AuNCs due to the enrichment effect of Ce-MOFs increasing the local concentration of Hg^{2+}. Thus, the high selectivity and sensitivity of Hg^{2+} detection can be achieved by assembling the specificality units (such as noble metals, and compounds with S) on MOFs. Under this guidance, in this study, Au was introduced to $Cu_3(BTC)_2$ through *in situ* reduction of $HAuCl_4$ by $Cu_xO@Cu_3(BTC)_2$, which was derived from $Cu_3(BTC)_2$. The oxidase-like activities of $CuO/Au@Cu_3(BTC)_2$ in the absence and presence of Hg^{2+} were investigated, and a colorimetric assay was constructed to detect Hg^{2+} based on the enhanced oxidase-like activity of $CuO/Au@Cu_3(BTC)_2$.

2. Experimental section

2.1 Reagent

Copper(II) nitrate trihydrate ($Cu(NO_3)_2\cdot 3H_2O$), methanol (CH_3OH), and hydrazine hydrate ($N_2H_4\cdot xH_2O$) were purchased from Shanghai Chemical Reagent Co., Ltd. Benzenetricarboxylic acid (BTC, $C_6H_3(CO_2H)_3$), gold chloride trihydrate ($HAuCl_4\cdot 3H_2O$), 3,3′, 5,5′-tetramethylbenzidine (TMB), sodium acetate (NaAc) and acetic acid (HAc) were purchased from Shanghai Aladdin Biochemical Technology Co., Ltd. All the reagents were used directly without further purification.

2.2 Preparation of samples

2.2.1 Preparation of $Cu_3(BTC)_2$. Typically, 1691.2 mg of $Cu(NO_3)_2\cdot 3H_2O$ and 882.6 mg of BTC were dissolved in 50 mL of methanol. Then, the $Cu(NO_3)_2$ solution was added to the BTC solution quickly under stirring at room temperature. After reacting for two hours, the blue precipitates were filtered through a 220 nm filter membrane, washed several times with methanol, and then vacuum dried at 60 °C for 6 hours.

2.2.2 Preparation of $Cu_xO@Cu_3(BTC)_2$. First, 1000 mg of $Cu_3(BTC)_2$ was dispersed in 500 mL of methanol by ultrasonication. Subsequently, 4.2 g of hydrazine hydrate was added to the above solution quickly. After stirring for 25 minutes at room temperature, 100 mL of deionized water was added to the solution with further stirring for 5 minutes. The brown precipitates were filtered through a 220 nm filter membrane and washed several times with methanol and deionized water, and then vacuum dried at 60 °C for 6 hours.

2.2.3 Preparation of $CuO/Au@Cu_3(BTC)_2$. Briefly, 50 mg of $Cu_xO@Cu_3(BTC)_2$ was dispersed in 200 mL of methanol by ultrasonication. Then, 200 μL of $HAuCl_4$ (100 mg mL^{-1}) solution was introduced to the above solution. After stirring for 120 minutes, the precipitates were filtered through a 220 nm filter membrane and washed several times with methanol, and then vacuum dried at 60 °C for 6 hours.

2.3 Oxidase-mimic activity and steady-state kinetics

The oxidase-mimic activities were evaluated by measuring the absorbance of ox-TMB at 652 nm. The experiments were conducted as follows: 100 μL of a HAc–NaAc (0.2 M, pH 3.6) buffer solution, 50 μL of a nanozyme suspension (1 mg mL^{-1}), with or without 2 μL of Hg^{2+} (0.01 M), were added to a testing tube. After adding 50 μL of TMB (20 mM), the solution was diluted to 2 mL with H_2O. After incubating for 5 minutes, UV-vis adsorption spectra were collected.

The steady-state kinetic experiments of $CuO/Au@Cu_3(BTC)_2$ in the presence of Hg^{2+} were carried out by changing the concentration of TMB at similar conditions, as described above. 100 μL of HAc–NaAc (0.2 M, pH 3.6) buffer solution, 50 μL of $CuO/Au@Cu_3(BTC)_2$ (1 mg mL^{-1}) and 2 μL of Hg^{2+} (0.01 M) were added to a testing tube. After adding different amounts of TMB, the solution was diluted to 2 mL with H_2O. The final concentration of TMB changed from 0.04 mM to 0.6 mM. Then, the absorbance at 652 nm *versus* time was monitored. The initial velocity and concentration of TMB were fitted with the Michaelis–Menten equation: $v = \frac{V_{max}\times[S]}{K_m+[S]}$, V_{max} and K_m were calculated through the Lineweaver–Burk plot: $\frac{1}{v} = \frac{K_m}{V_{max}}\frac{1}{[S]} + \frac{1}{V_{max}}$, where v refers to the initial velocity of the reaction, [S] is the concentration of substrate, V_{max} is the max velocity, and K_m is the Michaelis–Menten constant.

Trapping tests for $CuO/Au@Cu_3(BTC)_2$ in the presence of Hg^{2+} were carried out similarly to those described above. 100 μL of a HAc–NaAc (0.2 M, pH 3.6) buffer solution, 50 μL of a nanozyme suspension (1 mg mL^{-1}), 2 μL of Hg^{2+} (0.01 M) and a certain amount of reactive oxygen species (ROS) scavengers (*p*-benzoquinone, or β-carotene, or *tert*-butanol) were added to a testing tube. After adding 50 μL of TMB (20 mM), the solution was diluted to 2 mL with H_2O. The final concentration of the ROS scavenger was 5 mM. After incubating for 5 minutes, the UV-vis adsorption spectra were collected.

2.4 Colorimetric detection of Hg^{2+}

Typically, 100 μL of HAc–NaAc (0.2 M, pH 3.6) a buffer solution, 50 μL of $CuO/Au@Cu_3(BTC)_2$ (1 mg mL^{-1}) and Hg^{2+} with different concentrations were added to a testing tube. Then 50 μL of TMB (20 mM) was added. The final volume of solution was 2 mL by diluting with H_2O. After incubating for 5 minutes, the UV-vis adsorption spectra were collected.

2.5 Characterizations

X-ray diffraction (XRD) patterns were collected with a step size of 0.02° ranging from 5 to 80° from an X-ray diffractometer (X'Pert Pro MPD) with Cu Kα radiation (λ = 0.1543 nm). The transmission electron microscopy (TEM) and high-resolution transmission electron microscopy (HRTEM) images were taken from a HRTEM (JEM-2100UHR) equipped with an energy-dispersive X-ray spectroscope (EDX). X-ray photoelectron spectroscopy (XPS) data were acquired from a Thermo Fisher ESCALAB 250 spectrometer with Al Kα radiation and the binding energies were calibrated by the C1s peak (284.8 eV). All

the UV-vis absorption spectra were recorded on a U-T6A UV-vis spectrophotometer (Yipu, Shanghai).

3. Results and discussion

3.1 Characterization of CuO/Au@$Cu_3(BTC)_2$

The synthesis process of CuO/Au@$Cu_3(BTC)_2$ is illustrated in Scheme 1. Firstly, Cu^{2+} was coordinated with BTC in methanol to form $Cu_3(BTC)_2$, which then was reduced by hydrazine hydrate to produce $Cu_xO@Cu_3(BTC)_2$. After the reduction of Au^{3+} by $Cu_xO@Cu_3(BTC)_2$, CuO/Au@$Cu_3(BTC)_2$ was obtained. The crystal structures of the as-prepared samples were analyzed by XRD. As shown in Fig. 1(a), in the XRD pattern of Cu_x-O@$Cu_3(BTC)_2$, the diffraction peaks at 32.5°, 35.5°, 38.8°, 48.7°, 53.5°, 58.3°, 61.5°, 66.3°, 68.2°, 72.3° and 75.3° were indexed to the (110), (11−1), (111), (20−2), (020), (202), (11−3), (31−1), (220), (311) and (22−2) planes of the monoclinic CuO (PDF#48-1548), and the diffraction peaks at 36.4° and 42.3° belonged to the (111) and (200) planes of the cubic Cu_2O (PDF#05-0667).[34,35] While in the XRD pattern of CuO/Au@$Cu_3(BTC)_2$, no obvious diffraction peak of Cu_2O was detected. Besides the diffraction peaks of monoclinic CuO (PDF#48-1548), new peaks that appeared at 38.2°, 44.4°, 64.6°, and 77.5° were indexed to (111), (200), (220) and (311) planes of cubic Au (PDF#04-0784).[36] Additionally, compared with the XRD pattern of $Cu_3(BTC)_2$, no similar diffraction peaks were detected in $Cu_xO@Cu_3(BTC)_2$ and CuO/Au@$Cu_3(BTC)_2$. These results indicate that Cu^{2+} in $Cu_3(BTC)_2$ was reduced to CuO and Cu_2O, Cu_2O further reduced Au^{3+} to Au during the preparation process of CuO/Au@Cu_3(-$BTC)_2$, and the crystal structure of $Cu_3(BTC)_2$ was disrupted during the reduction process.

XPS was employed to further determine the chemical composition of CuO/Au@$Cu_3(BTC)_2$. As shown in Fig. 1(b), Cu2p, Au4f, O1s, and C1s signals appeared in the full XPS spectra, with corresponding contents of 32.63 at%, 0.36 at%, 43.02 at% and 23.99 at%, respectively. Moreover, the C1s signal peak (Fig. 1(c)) was deconvoluted to two peaks, which was attributed to C–C (284.8 eV) and O–C=O (288.3 eV), indicating that the C element in the CuO/Au@$Cu_3(BTC)_2$ came from BTC in $Cu_3(BTC)_2$.[37] Furthermore, the O1s signal peak (Fig. 1(d)) was deconvoluted into three peaks. The binding peaks at 529.7 and 531.1 eV were assigned to the lattice oxygen (O_L) and oxygen vacancies (O_V) of CuO, respectively, and the binding peak at 531.8 eV was assigned to the C–O/C=O bond of BTC in $Cu_3(BTC)_2$.[38–40] The above results indicate that $Cu_3(BTC)_2$ was still retained in the CuO/Au@$Cu_3(BTC)_2$ sample. Additionally, the Cu2p spectrum (Fig. 1(e)) displayed two binding peaks at 933.8 and 953.5 eV, corresponding to the $Cu2p_{3/2}$ and $Cu2p_{1/2}$ orbits of Cu(II), respectively.[38,39] The Au4f spectrum (Fig. 1(f)) displayed two binding peaks that appeared at 84.2 and 87.9 eV, corresponding to the $Au4f_{7/2}$ and $Au4f_{5/2}$ orbits of Au(0), respectively.[41] Combining XRD and XPS results, it can be concluded that the as-prepared CuO/Au@$Cu_3(BTC)_2$ was composed of CuO, Au, and $Cu_3(BTC)_2$.

The morphology of CuO/Au@$Cu_3(BTC)_2$ was characterized by TEM and HRTEM. As shown in Fig. 2(a) and (b), the structure of CuO/Au@$Cu_3(BTC)_2$ exhibited a relatively transparent $Cu_3(BTC)_2$ substrate and a large number of nanoparticles. The HRTEM image in Fig. 2(c) exhibited that the nanoparticles were composed of multiple nanocrystals. The lattice distances of 0.19, 0.23, and 0.25 nm were attributed to the (20−2), (111), and (11−1) lattice planes of monoclinic CuO, respectively.[42] Furthermore, the lattice distances of 0.21 and 0.24 nm were attributed to the (200) and (111) lattice planes of cubic Au, respectively.[43] In addition, the EDX mapping images (Fig. 2(c)–(i)) displayed that the C, O, Cu, and Au elements were distributed uniformly throughout CuO/Au@$Cu_3(BTC)_2$. These results were consistent with the XRD and XPS results, further confirming the successful synthesis of CuO/Au@$Cu_3(BTC)_2$.

3.2 Oxidase-mimic activity and steady-state kinetics

The oxidase-mimic activity of the synthesized nanozymes was evaluated by measuring the color change of TMB with nanozymes. Under the catalysis of nanozymes, colorless TMB was oxidized to blue ox-TMB with the help of O_2. As shown in Fig. 3(a), almost no color change was observed in all the materials before the addition of Hg^{2+}, and no obvious absorption peaks appeared on the absorption spectra. After the addition of Hg^{2+}, only CuO/Au@$Cu_3(BTC)_2$-TMB had a clear absorption peak at 652 nm, and the color also changed to deep blue. Moreover, according to the time-dependent absorbance changes at 652 nm in Fig. S1,† the oxidation of TMB under the catalysis of CuO/Au@$Cu_3(BTC)_2$ proceeded quickly in the presence of Hg^{2+} and reached equilibrium within 2 minutes. The results demonstrate that Hg^{2+} can significantly enhance the oxidase-mimic activity of CuO/Au@$Cu_3(BTC)_2$.

The influences of the testing conditions on the catalytic activity of TMB oxidation with CuO/Au@$Cu_3(BTC)_2$ in the presence of Hg^{2+} were investigated by measuring the absorbance of ox-TMB at 652 nm. Generally, the reaction of TMB

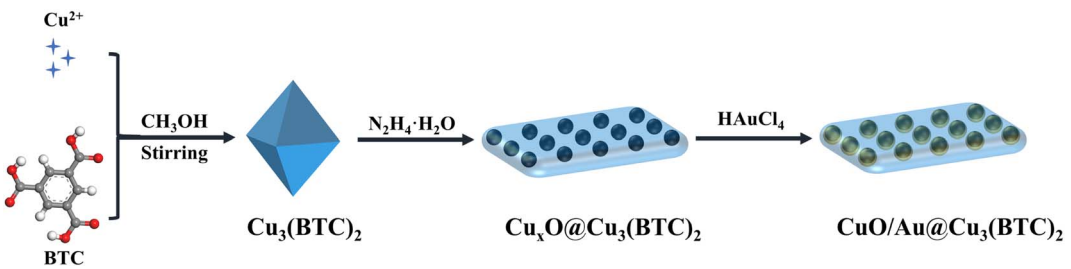

Scheme 1 Schematic illustration of the synthesis process of CuO/Au@$Cu_3(BTC)_2$.

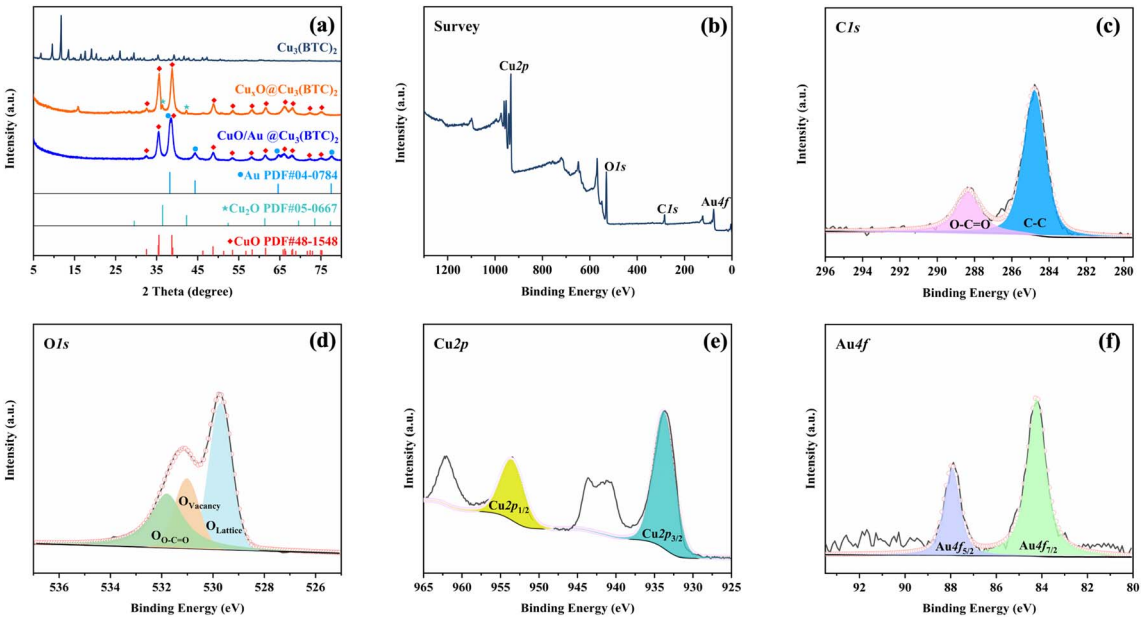

Fig. 1 (a) XRD patterns of the as-prepared samples, (b) survey, (c) C1s, (d) O1s, (e) Cu2p, and (f) Au4f XPS spectra of the CuO/Au@$Cu_3(BTC)_2$ sample.

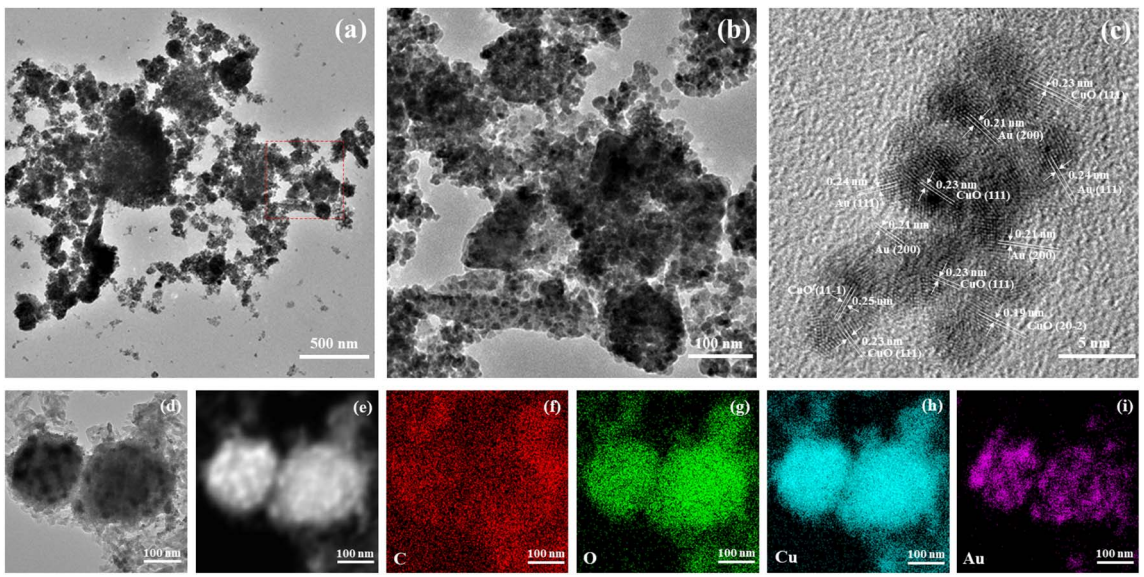

Fig. 2 Morphology characterizations of the CuO/Au@$Cu_3(BTC)_2$ sample. (a) TEM image, (b) partial magnification in (a), (c) HRTEM image, and (d–i) EDX-mapping images.

losing one electron to generate ox-TMB is favorable in acidic conditions. Therefore, pH can seriously affect the catalytic activity. As shown in Fig. S2(a),† the absorbance at 652 nm (A_{652}) changed little at pH ranging from 3 to 6, implying CuO/Au@$Cu_3(BTC)_2$ exhibited a good catalytic performance over a relatively wide pH range. In addition, the effect of temperature on the catalytic activity of nanozymes was considered. After incubating at different temperatures ranging from 10 to 60 °C, A_{652} of the sensing system was recorded (Fig. S2(b)†). As the temperature increased, A_{652} increased first and then decreased, and reached a maximum at 20 °C. This interesting trend might be caused by the decrease in reaction rate at low temperatures and a decrease in dissolved oxygen in water at high temperatures. It is worth noting that even at 60 °C A_{652} remained at 70.8% of the max. The results demonstrate that the CuO/Au@$Cu_3(BTC)_2$-TMB-Hg^{2+} sensing system can be conducted under wide testing conditions, which is beneficial for practical applications.

Steady-state kinetic experiments were carried out by changing the TMB concentration to further elucidate the

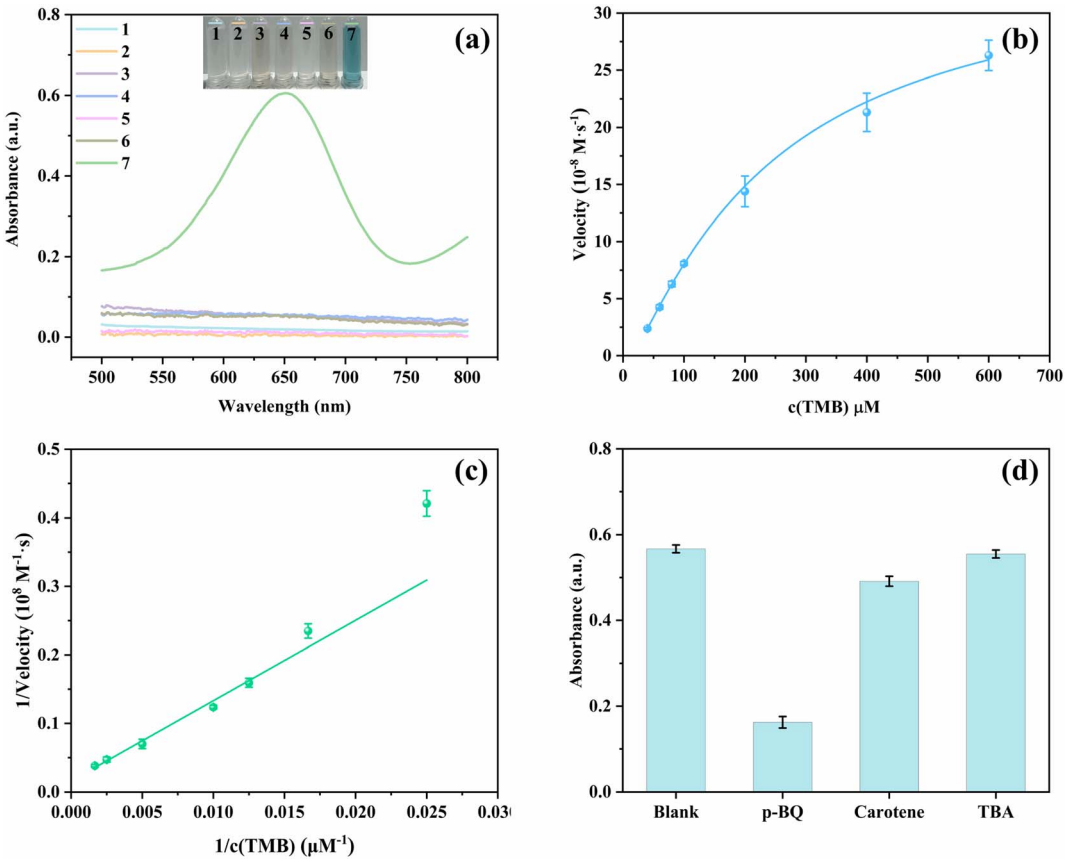

Fig. 3 (a) UV-vis absorbance spectra of (1) Hg^{2+}-TMB, (2) $Cu_3(BTC)_2$-TMB, (3) $Cu_xO@Cu_3(BTC)_2$-TMB, (4) CuO/Au@$Cu_3(BTC)_2$-TMB, (5) $Cu_3(BTC)_2$-Hg^{2+}-TMB, (6) $Cu_xO@Cu_3(BTC)_2$-Hg^{2+}-TMB, (7) CuO/Au@$Cu_3(BTC)_2$-Hg^{2+}-TMB; inset shows the responding photos. (b) Michaelis–Menten curve and (c) corresponding Lineweaver–Burk plotting curve of CuO/Au@$Cu_3(BTC)_2$-Hg^{2+}-TMB. (d) Absorbance at 652 nm of CuO/Au@$Cu_3(BTC)_2$-Hg^{2+}-TMB with different radical scavengers.

enhanced oxidase-mimic activity of CuO/Au@$Cu_3(BTC)_2$ triggered by Hg^{2+}. As shown in Fig. 3(b), a typical Michaelis–Menten curve was obtained between TMB concentration and initial velocity. By fitting the double reciprocal curve (Fig. 3(c)), V_{max} and K_m were calculated with the Lineweaver Burk equation to be 0.629 μM s^{-1} and 0.74 mM, respectively. As compared in Table S1,† the V_{max} in CuO/Au@$Cu_3(BTC)_2$-Hg^{2+}-TMB is larger than those of the others, implying an excellent catalytic activity.[44,45]

To investigate the catalytic mechanism of the oxidase-mimic activity of CuO/Au@$Cu_3(BTC)_2$ stimulated by Hg^{2+}, TEM and EDX-mapping images of CuO/Au@$Cu_3(BTC)_2$ after the addition of Hg^{2+} were analyzed and are displayed in Fig. S3.† From Fig. S3(f) and (g),† it is observed that Hg overlapped with Au well. In addition, energy-dispersive X-ray spectroscopies of $Cu_xO@Cu_3(BTC)_2$ before and after Hg^{2+} addition are compared in Fig. S4 and S5,† Hg appeared in the EDX spectroscopy after adding Hg^{2+}. The results proved that Hg^{2+} was reduced to Hg^0 by Au on CuO/Au@$Cu_3(BTC)_2$. The formed Au–Hg amalgam changed the surface property and thus enhanced the oxidase-mimic activity.[9,46] To further investigate the catalytic mechanism, KSCN was added into the sensing system. As shown in Fig. S6(a),† A_{652} decreased significantly after adding KSCN, indicating in this situation the catalytic activity of CuO/Au@$Cu_3(BTC)_2$ in the presence of Hg^{2+} was greatly inhibited. Moreover, the catalytic oxidation of TMB was conducted separately in the presence of N_2 and O_2. The catalytic mixture solution was bubbled with N_2 or O_2 for 10 minutes before TMB was added. After incubation for 5 min, UV-vis absorbance spectra were collected. As shown in Fig. S6(b),† A_{652} was significantly inhibited in N_2 and enhanced in O_2 compared with that in air, hinting that dissolved oxygen played an important role in the oxidase catalytic activity. Under the catalysis of CuO/Au@$Cu_3(BTC)_2$ in the presence of Hg^{2+}, O_2 was activated to produce ROS, which could oxidize TMB to ox-TMB. Then, trapping tests were carried out to confirm the active species. *p*-Benzoquinone (PBQ), β-carotene, and *tert*-butanol (TBA) were employed as scavengers for $O_2^{\bullet-}$, $^1O_2$, and $^{\bullet}OH$, respectively.[47] It was observed that the oxidization of TMB was apparently inhibited in the presence of PBQ and rarely changed with β-carotene and TBA (Fig. 3(d)), indicating that the active oxygen generated in this catalytic reaction was $O_2^{\bullet-}$ rather than $^1O_2$, and $^{\bullet}OH$. Therefore, for the catalytic mechanism of the oxidase-mimic activity of CuO/Au@$Cu_3(BTC)_2$ stimulated by Hg^{2+} it can be concluded that the Au–Hg alloy generated by the reaction of $Hg^{2+}$and Au in CuO/Au@$Cu_3(BTC)_2$ could activate O_2 to $O_2^{\bullet-}$, thereby catalyzing the oxidation of TMB to be blue ox-TMB.

3.3 Colorimetric detection of Hg^{2+} and selectivity

Benefiting from the enhanced oxidase-mimic activity of CuO/Au@$Cu_3(BTC)_2$ triggered by Hg^{2+}, a colorimetric sensing method was designed for Hg^{2+} detection. As displayed in Fig. 4(a) and (b), an augmentation in A_{652} was noticed with the increase of Hg^{2+} concentration, along with the color change from colorless to blue. A good linear relationship between A_{652} and Hg^{2+} concentration was gained in the range of 0.05–25 μM. The linear equation is $A = 0.08228 + 0.04927c$ ($R^2 = 0.99914$), and the limit of detection (LOD) was calculated to be 9.7 nM according to the $3\sigma/s$ rule, where σ is the standard deviation of the blank and s is the slope of the linear equation. Compared with previously reported methods (Table S2†), the colorimetric assay in this work provided a comparable detection range and LOD, suggesting its excellent potential for Hg^{2+} detection.

To evaluate the specificity and selectivity, common cations (Na^+, K^+, NH_4^+, Ca^{2+}, Mg^{2+}, Cu^{2+}, Fe^{2+}, Co^{2+}, Ni^{2+}, Cd^{2+}, Pb^{2+}, Cr^{3+}) and anions (Cl^-, F^-, Br^-, NO_3^-, HCO_3^-, CO_3^{2-}, SO_4^{2-}, HPO_4^{2-}) were added to the CuO/Au@$Cu_3(BTC)_2$-TMB system instead of Hg^{2+}. The results depicted in Fig. 4(d) and (e) informed that slight absorbance changes were observed with interference ions even when the concentration was ten times that of Hg^{2+}, indicating that the CuO/Au@$Cu_3(BTC)_2$-TMB system shows a good selectivity to Hg^{2+}.

To further verify the practicality of colorimetric detection of Hg^{2+} based on the CuO/Au@$Cu_3(BTC)_2$-TMB system, tap water was chosen for measurement and filtered with a 220 nm filter membrane before being used. According to the standard addition method, the recoveries and relative standard deviation (RSD) were calculated and are listed in Table 1. The recovery of the proposed method for Hg^{2+} detection is between 93.8% and 107.5% with a RSD of no more than 5%, demonstrating the feasibility in practical application.

Table 1 Recovery tests for Hg^{2+} detection in real water samples

Samples	Added (μM)	Found (μM)	Recovery (%)	RSD (%, $n = 3$)
Tap water	2	2.1	105	1.5
	4	4.3	107.5	1.6
	8	7.5	93.8	4.5

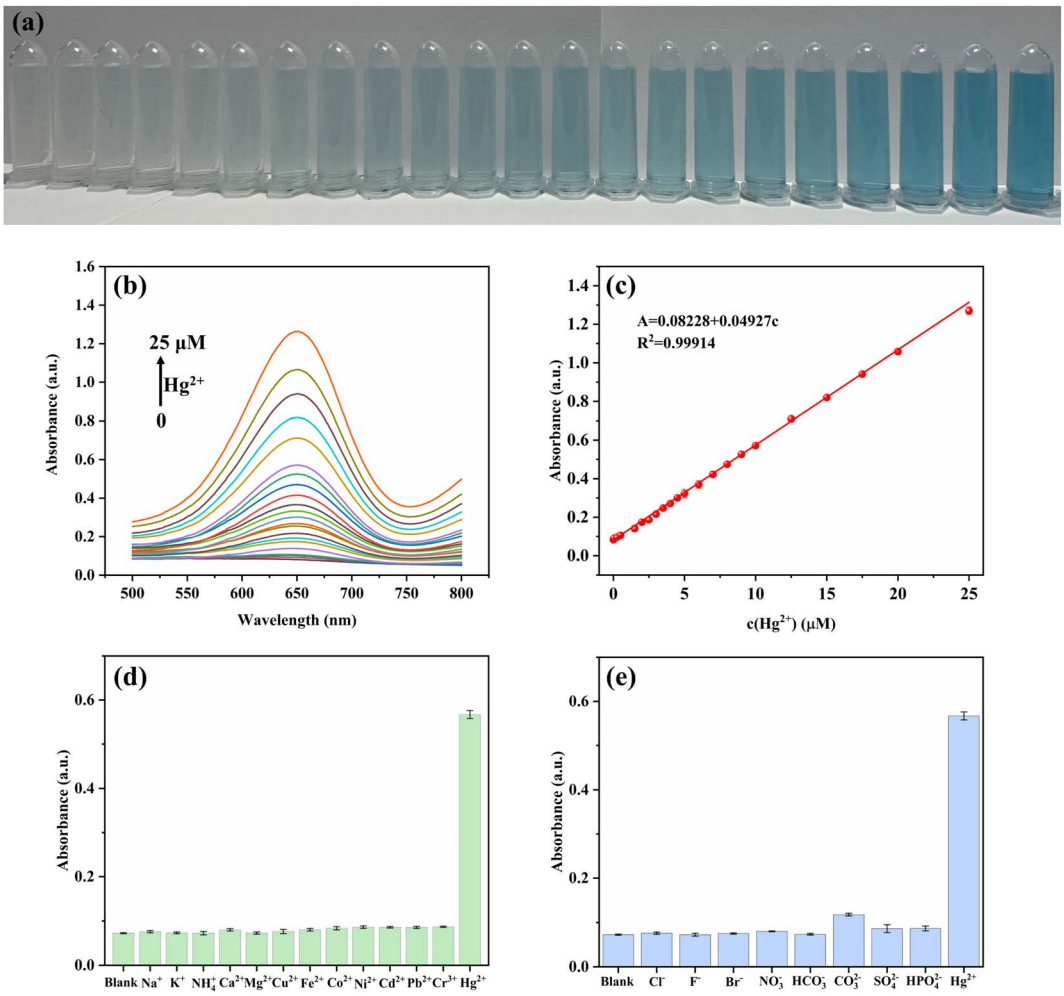

Fig. 4 (a) Photo and (b) UV-vis spectra of the colorimetric response of CuO/Au@$Cu_3(BTC)_2$-TMB to different concentrations of Hg^{2+}. (c) Calibration curve of A_{652} *versus* concentration of Hg^{2+}, (d) and (e) are selectivity responses of CuO/Au@$Cu_3(BTC)_2$-TMB to Hg^{2+} (10 μM) and the interference ions (0.1 mM).

4. Conclusion

In summary, $CuO/Au@Cu_3(BTC)_2$ nanomaterials were successfully prepared through the reduction of $HAuCl_4$ by Cu_x-$O@Cu_3(BTC)_2$, which was derived from $Cu_3(BTC)_2$, and exhibited an enhanced oxidation-like activity triggered by Hg^{2+} through forming a Au–Hg amalgam. In the presence of Hg^{2+}, $CuO/Au@Cu_3(BTC)_2$ could catalyze O_2 to generate $O_2^{\bullet-}$, oxidizing the colorless TMB to blue ox-TMB within 5 min. Therefore, a colorimetric sensing method was designed for Hg^{2+} detection based on this phenomenon. A good linearity was obtained in the 0.05–25 μM range, with a LOD of 9.7 nM. Moreover, the sensing strategy exhibited an excellent selectivity to Hg^{2+} and good recoveries in tap water. The high sensitivity and selectivity and rapid response in this sensing system show its potential for Hg^{2+} detection in practical applications, which will promote the application of nanozymes in heavy ion detection in environmental analysis.

Author contributions

Min Yang: data analysis, investigation, original draft writing, methodology, writing – review & editing; Jian Wang: images analysis, methodology, writing – review & editing; Xuan Xue: formal analysis, investigation; Hechun Jiang: supervision, review and editing.

Conflicts of interest

There are no conflicts to declare.

Acknowledgements

This work was financially supported by the Natural Science Research Project of Universities in Anhui Province (No. KJ2020A0414) and Talent Support Program of Anhui University of Traditional Chinese Medicine (No. 2023rcyb029).

References

1 H. Xie, X. Yang, J. Xu and D. Zhong, Heavy metals pollution and potential ecological health risk assessment in the Yangtze River reaches, *J. Environ. Chem. Eng.*, 2023, **11**, 109489.
2 G. Yu, L. Wu, Q. Su, X. Ji, J. Zhou, S. Wu, Y. Tang and H. Li, Neurotoxic effects of heavy metal pollutants in the environment: focusing on epigenetic mechanisms, *Environ. Pollut.*, 2024, **345**, 123563.
3 M. Li, X. Li, M. Xu, B. Liu, M. Yang, Z. Chen, T. Gao, T. D. James, L. Wang and H. Xiao, A ratiometric fluorescent hydrogel of controlled thickness prepared continuously using microtomy for the detection and removal of Hg(II), *Chem. Eng. J.*, 2021, **426**, 131296.
4 S. Hu, Y. Zhang, H. Meng, Y. Yang, G. Chen, Q. Wang, K. Cheng, C. Guo, X. Li and T. Liu, Transformation and migration of Hg in a polluted alkaline paddy soil during flooding and drainage processes, *Environ. Pollut.*, 2024, **345**, 123471.
5 L. Mao, W. Ren, Y. Tang, X. Liu, M. He, K. Sun, B. Zhang, C. Lin and W. Ouyang, Comprehensive insight into mercury contamination in atmospheric, terrestrial and aquatic ecosystems surrounding a typical antimony-coal mining district, *J. Hazard. Mater.*, 2024, **469**, 133880.
6 T. Rasheed, C. Li, M. Bilal, C. Yu and H. M. N. Iqbal, Potentially toxic elements and environmentally-related pollutants recognition using colorimetric and ratiometric fluorescent probes, *Sci. Total Environ.*, 2018, **640–641**, 174–193.
7 J. Li, W. Peng, A. Wang, M. Wan, Y. Zhou, X. Zhang, S. Jin and F. Zhang, Highly sensitive and selective SERS substrates with 3D hot spot buildings for rapid mercury ion detection, *Analyst*, 2023, **148**, 4044–4052.
8 M. Yin, Y. Wan, S. Li, X. Zhao, W. Zhang, Y. Zhang and H. Wang, Carbon nitride-doped melamine-silver adsorbents with peroxidase-like catalysis and visible-light photocatalysis: colorimetric detection and detoxification removal of total mercury, *J. Hazard. Mater.*, 2021, **408**, 124978.
9 G. Panthi and M. Park, Synthesis of metal nanoclusters and their application in Hg^{2+} ions detection: a review, *J. Hazard. Mater.*, 2022, **424**, 127565.
10 S. Chen, K. Jiang, Y. Liang, J. He, B. Xu, Z. Chen and Z. Wang, Fine-tuning benzazole-based probe for the ultrasensitive detection of Hg^{2+} in water samples and seaweed samples, *Food Chem.*, 2023, **428**, 136800.
11 Y. Lv, L. Yang, X. Mao, M. Lu, J. Zhao and Y. Yin, Electrochemical detection of glutathione based on Hg^{2+}-mediated strand displacement reaction strategy, *Biosens. Bioelectron.*, 2016, **85**, 664–668.
12 X. Guo, F. Chen, F. Wang, Y. Wu, Y. Ying, Y. Wen, H. Yang and Q. Ke, Recyclable Raman chip for detection of trace mercury ions, *Chem. Eng. J.*, 2020, **390**, 124528.
13 J. Hu, D. Wang, L. Dai, G. Shen and J. Qiu, Application of fluorescent biosensors in the detection of Hg(II) based on T-Hg(II)-T base pairs, *Microchem. J.*, 2020, **159**, 105562.
14 N. Ma, X. Ren, H. Wang, X. Kuang, D. Fan, D. Wu and Q. Wei, Ultrasensitive controlled release aptasensor using thymine–Hg^{2+}–thymine mismatch as a molecular switch for Hg^{2+} detection, *Anal. Chem.*, 2020, **92**, 14069–14075.
15 D. Dai, J. Yang, Y. Wang and Y. Yang, Recent progress in functional materials for selective detection and removal of mercury(II) ions, *Adv. Funct. Mater.*, 2021, **31**, 2006168.
16 T. Samanta, N. Das, D. Patra, P. Kumar, B. Sharmistha and R. Shunmugam, Reaction-triggered ESIPT active water-soluble polymeric probe for potential detection of Hg^{2+}/CH_3Hg^+ in both environmental and biological systems, *ACS Sustain. Chem. Eng.*, 2021, **9**, 5196–5203.
17 L. Yao, Y. Chen, R. Wang, C. Yan, J. Xu, B. Yao, J. Cheng and W. Chen, Rapid and sensitive detection of Hg^{2+} with a SERS-enhanced lateral flow strip, *Analyst*, 2022, **147**, 4337–4347.
18 K. Liu, L. Marin and X. Cheng, Water-soluble β-cyclodextrin based turn-on amplifying fluorescent probes for sensitive

and selective detection of Hg^{2+}/Hg^{+} ions, *Sens. Actuators, B*, 2023, **377**, 133060.

19 Q. Ran, H. Feng, G. Chang, M. Luo and S. Xu, Thymine-mediated electrochemical aptasensor for sensitive and simultaneous detection of Hg^{2+} and CH_3Hg^{+} in fish samples, *Electrochim. Acta*, 2023, **461**, 142406.

20 L. Zhang, X. Bi, H. Wang, L. Li and T. You, Loading of AuNCs with AIE effect onto cerium-based MOFs to boost fluorescence for sensitive detection of Hg^{2+}, *Talanta*, 2024, 125843.

21 Y. Ma, Y. Yu, X. Mu, C. Yu, Y. Zhou, J. Chen, S. Zheng and J. He, Enzyme-induced multicolor colorimetric and electrochemiluminescence sensor with a smartphone for visual and selective detection of Hg^{2+}, *J. Hazard. Mater.*, 2021, **415**, 125538.

22 L. Kong, C. Wang, W. Yang, L. Zhou and S. Wei, The ultrathin palladium nanosheets for sensitive and visual Hg^{2+} detection in the food chain, *J. Hazard. Mater.*, 2022, **427**, 128135.

23 J. Jiang and X. Kan, Mimetic peroxidase based on a gold amalgam for the colorimetric sensing of trace mercury(II) in water samples, *Analyst*, 2022, **147**, 2388–2395.

24 H. A. A. Noreldeen, L. Yang, X. Guo, S. He, H. Peng, H. Deng and W. Chen, A peroxidase-like activity-based colorimetric sensor array of noble metal nanozymes to discriminate heavy metal ions, *Analyst*, 2022, **147**, 101–108.

25 T. Liu, Y. Li, J. Gu, L. Zhang, F. Qian, B. Li and X. Wang, Achieving smartphone-based colorimetric assay for Hg^{2+} with a bimetallic site strategy based on Hg^{2+}-triggered oxidase-like catalytic activity of NSC/$Co_6Ni_3S_8$ nanocomposite, *Anal. Chim. Acta*, 2023, **1278**, 341734.

26 L. Luo, C. Xi, J. Zhuo, G. Liu, S. Yang, Y. Nian, J. Sun, M. Zhu and J. Wang, A portable dual-mode colorimetric platform for sensitive detection of Hg^{2+} based on $NiSe_2$ with Hg^{2+}-activated oxidase-like activity, *Biosens. Bioelectron.*, 2022, **215**, 114519.

27 R. Li, X. He, R. Javed, J. Cai, H. Cao, X. Liu, Q. Chen, D. Ye and H. Zhao, Switching on-off-on colorimetric sensor based on Fe-N/S-C single-atom nanozyme for ultrasensitive and multimodal detection of Hg^{2+}, *Sci. Total Environ.*, 2022, **834**, 155428.

28 Y. Cai, J. Wang, L. Niu, Y. Zhang, X. Liu, C. Liu, S. Yang, H. Qi and A. Liu, Selective colorimetric sensing of sub-nanomolar Hg^{2+} based on its significantly enhancing peroxidase mimics of silver/copper nanoclusters, *Analyst*, 2021, **146**, 4630–4635.

29 K. Xiang, G. Chen, A. Nie, W. Wang and H. Han, Silica-based nanoenzymes for rapid and ultrasensitive detection of mercury ions, *Sens. Actuators, B*, 2021, **330**, 129304.

30 A. Shahat, S. A. Elsalam, J. M. Herrero-Martínez, E. F. Simó-Alfonso and G. Ramis-Ramos, Optical recognition and removal of Hg(II) using a new self-chemosensor based on a modified amino-functionalized Al-MOF, *Sens. Actuators, B*, 2017, **253**, 164–172.

31 L. Fu, K. Xie, A. Wang, F. Lyu, J. Ge, L. Zhang, H. Zhang, W. Su, Y. Hou, C. Zhou, C. Wang and S. Ruan, High selective detection of mercury (II) ions by thioether side groups on metal-organic frameworks, *Anal. Chim. Acta*, 2019, **1081**, 51–58.

32 A. Pankajakshan, D. Kuznetsov and S. Mandal, Ultrasensitive detection of Hg(II) ions in aqueous medium using zinc-based metal-organic framework, *Inorg. Chem.*, 2019, **58**, 1377–1381.

33 B. Li, X. Xie, T. Meng, X. Guo, Q. Li, Y. Yang, H. Jin, C. Jin, X. Meng and H. Pang, Recent advance of nanomaterials modified electrochemical sensors in the detection of heavy metal ions in food and water, *Food Chem.*, 2024, **440**, 138213.

34 S. Ju, M. Yusuf, S. Jang, H. Kang, S. Kim and K. H. Park, Simple transformation of hierarchical hollow structures by reduction of metal-organic frameworks and their catalytic activity in the oxidation of benzyl alcohol, *Chem.–Eur. J.*, 2019, **25**, 7852–7859.

35 L. Wang, S. Li, Y. Chen and H. Jiang, Encapsulating copper nanocrystals into metal-organic frameworks for cascade reactions by photothermal catalysis, *Small*, 2021, **17**, 2004481.

36 D. Dai, H. Liu, H. Ma, Z. Huang, C. Gu and M. Zhang, In-situ synthesis of Cu_2OAu nanocomposites as nanozyme for colorimetric determination of hydrogen peroxide, *J. Alloys Compd.*, 2018, **747**, 676–683.

37 J. Wang, H. Liu, S. Fan, W. Li, Z. Li, H. Yun, X. Xu, A. Guo and Z. Wang, Size-dependent catalytic cyclohexane dehydrogenation with platinum nanoparticles on nitrogen-doped carbon, *Energy Fuels*, 2020, **34**, 16542–16551.

38 Q. Lian, H. Liu, X. Zheng, X. Li, F. Zhang and J. Gao, Enhanced peroxidase-like activity of CuO/Pt nanoflowers for colorimetric and ultrasensitive Hg^{2+} detection in water sample, *Appl. Surf. Sci.*, 2019, **483**, 551–561.

39 Q. Huang, Z. Deng, R. Zhang, A. Klamchuen, M. Horprathum, S. Wang, X. Fang, L. You, S. Huang and G. Meng, Highly sensitive and selective ppb-level ozone sensor based on porous CuO nanoparticles, *Sens. Actuators, B*, 2024, **406**, 135434.

40 M. Li, Y. Xie, J. Zhang and X. Su, Self-assembled integrated nanozyme cascade biosensor with dual catalytic activity for portable urease analysis, *Anal. Chem.*, 2024, **96**, 1284–1292.

41 G. Li, Y. Wu, C. Zhong, Y. Yang and Z. Lin, Predesigned covalent organic framework with sulfur coordination: Anchoring Au nanoparticles for sensitive colorimetric detection of Hg(II), *Chin. Chem. Lett.*, 2024, **35**, 108904.

42 D. Xu, C. Zhu, X. Meng, Z. Chen, Y. Li, D. Zhang and S. Zhu, Design and fabrication of Ag-CuO nanoparticles on reduced graphene oxide for nonenzymatic detection of glucose, *Sens. Actuators, B*, 2018, **265**, 435–442.

43 S. B. Lee, S. Kang, J. Jung, S. Sung, S. J. Yoo and H. N. Han, Lattice shear and non-random rotation of Au nanoparticles under electron-beam irradiation, *Acta Mater.*, 2022, **241**, 118387.

44 Y. Tao, E. Ju, J. Ren and X. Qu, Bifunctionalized mesoporous silica-supported gold nanoparticles: intrinsic oxidase and peroxidase catalytic activities for antibacterial applications, *Adv. Mater.*, 2015, **27**, 1097–1104.

45 Y. Wang, Z. Zhang, G. Jia, L. Zheng, J. Zhao and X. Cui, Elucidating the mechanism of the structure-dependent

enzymatic activity of Fe–N/C oxidase mimics, *Chem. Commun.*, 2019, **55**, 5271–5274.

46 F. Kong, L. Yao, X. Lu, H. Li, Z. Wang, H. Fang and W. Wang, Au-Hg/rGO with enhanced peroxidase-like activity for sensitive colorimetric determination of H_2O_2, *Analyst*, 2020, **145**, 2191–2196.

47 Y. Chen, Q. Tian, H. Wang, R. Ma, R. Han, Y. Wang, H. Ge, Y. Ren, R. Yang, H. Yang, Y. Chen, X. Duan, L. Zhang, J. Gao, L. Gao, X. Yan and Y. Qin, A manganese-based metal-organic framework as a cold-adapted nanozyme, *Adv. Mater.*, 2024, **36**, 2206421.